Second-order sliding-mode-based global control scheme for wind turbine-driven DFIGs subject to unbalanced and distorted grid voltage

Miren Itsaso Martinez, Ana Susperregui, Gerardo Tapia

Second-order sliding-mode-based global control scheme for wind turbine-driven DFIGs subject to unbalanced and distorted grid voltage

Miren Itsaso Martinez[1,*], Ana Susperregui[1], Gerardo Tapia[1]

[1]University of the Basque Country UPV/EHU; Department of Automatic Control and Systems Engineering; Faculty of Engineering, Gipuzkoa; Plaza de Europa, 1; 20018 San Sebastián; Spain
[*]Email: mirenitsaso.martinez@ehu.eus

Abstract: Control algorithms for both the rotor- and grid-side power converters of a wind turbine-driven doubly-fed induction generator (DFIG) are detailed, and tuning equations are also provided to assist adjustment of their gains and constants. Those algorithms are based on the second-order sliding-mode control (2-SMC) approach, and they allow the wind turbine to satisfactorily operate under grid voltage non-idealities, such as simultaneously distorted and unbalanced scenarios. The presented solution turns out to be robust against parameter deviations and disturbances, and of high-performance dynamic response. Moreover, it drives the transistors of both power converters at a constant switching frequency, also avoiding decomposition in symmetrical sequences of either the grid voltage or currents. The controllers proposed for the two power converters are validated through experimentation on a 7-kW DFIG test bench subject to a significantly unbalanced and harmonically distorted grid voltage. Their robustness in the presence of both substantial parameter mismatch and disturbances attributable to wind variability is also assessed.

1. Nomenclature

C	DC-link capacitance
e_n	component of grid voltage space-vector
$\boldsymbol{e}_n$	grid voltage space-vector
f_r and f_s	rotor electrical and synchronous frequencies
i_g, i_r and i_s	components of grid-side, rotor and stator current space-vectors
$\boldsymbol{i}_g, \boldsymbol{i}_r$ and $\boldsymbol{i}_s$	grid-side, rotor and stator current space-vectors
L_g	line filter inductance
L_{lr} and L_{ls}	rotor and stator leakage inductances
L_m, L_r and L_s	magnetising, rotor and stator inductances
n	stator-to-rotor effective turns ratio
P	number of pole pairs
P_g and Q_g	grid-side converter (GSC) output active and reactive powers
P_r and Q_r	rotor active and reactive powers
P_s and Q_s	stator active and reactive powers
P_t and Q_t	total active and reactive powers from the overall generating unit
R_g, R_r and R_s	line filter, rotor and stator resistances
T_e	electromagnetic torque

v_{DC}	DC-link voltage
v_g and v_r	components of GSC and rotor-side converter (RSC) output voltage space-vectors
$\boldsymbol{v}_g$ and $\boldsymbol{v}_r$	GSC and RSC output voltage space-vectors
v_s	component of stator voltage space-vector
$\boldsymbol{v}_s$	stator voltage space-vector
ω_r and ω_{rm}	rotor electrical and mechanical angular speeds
ω_s	synchronous angular frequency
ψ_s	component of stator magnetic flux space-vector
$\boldsymbol{\psi}_r$ and $\boldsymbol{\psi}_s$	rotor and stator magnetic flux space-vectors

Subscripts

d and q	direct- and quadrature-axis components, expressed in the stationary reference frame
T_e, Q_s	variable or parameter associated with the electromagnetic torque and stator reactive power
P_g, Q_g	variable or parameter associated with the grid-side active and reactive powers
1	variable associated with the primary-side of the transformer installed at the laboratory test bench

Superscripts

$*$	set-point or reference value

2. Introduction

Multimegawatt wind turbine systems constitute the backbone of renewable energy-based power generation [1]. On the other hand, severe and random disturbances —e.g. harmonic distortion, imbalances— may occur in the grid to which such wind energy conversion systems are connected, with durations that may vary from a fraction of a cycle to a few cycles [2].

Voltage source converters (VSCs) are mainly used as active interface between electric generators and the grid. With the growing in renewables, a strong research effort has been devoted, during the last more than ten years, to development of control algorithms that allow VSCs to deal with the afore-cited grid disturbances [3].

Most of the wind turbine-driven generators comprise two three-phase VSCs, linked to each other by a DC bus. Thus, the electric generator is generally decoupled from the grid, and, consequently, the capability to deal with grid disturbances is only required for the grid-side converter (GSC) control system. However, the wind turbine-driven doubly-fed induction generator (DFIG) represents a particular case in which the stator of the electric generator is directly connected to the grid, as depicted in Fig. 1*a*. As a consequence, not only the GSC but also the rotor-side converter (RSC) needs to be provided with an advanced control algorithm, specifically conceived to avoid occurrence of undesirable effects due to grid disturbances —e.g. oscillations in the electromagnetic torque, DC-link voltage, and active and reactive powers.

Proportional-integral (PI) and PI+resonant (PI+R) controller-based schemes were firstly proposed to cope either with unbalanced —[4]–[8]— or distorted —[9], [10]— grid voltage scenarios. The main drawbacks reported for those schemes are low-performance transient response, poor system stability, the need for extracting positive and negative sequences or/and harmonic components
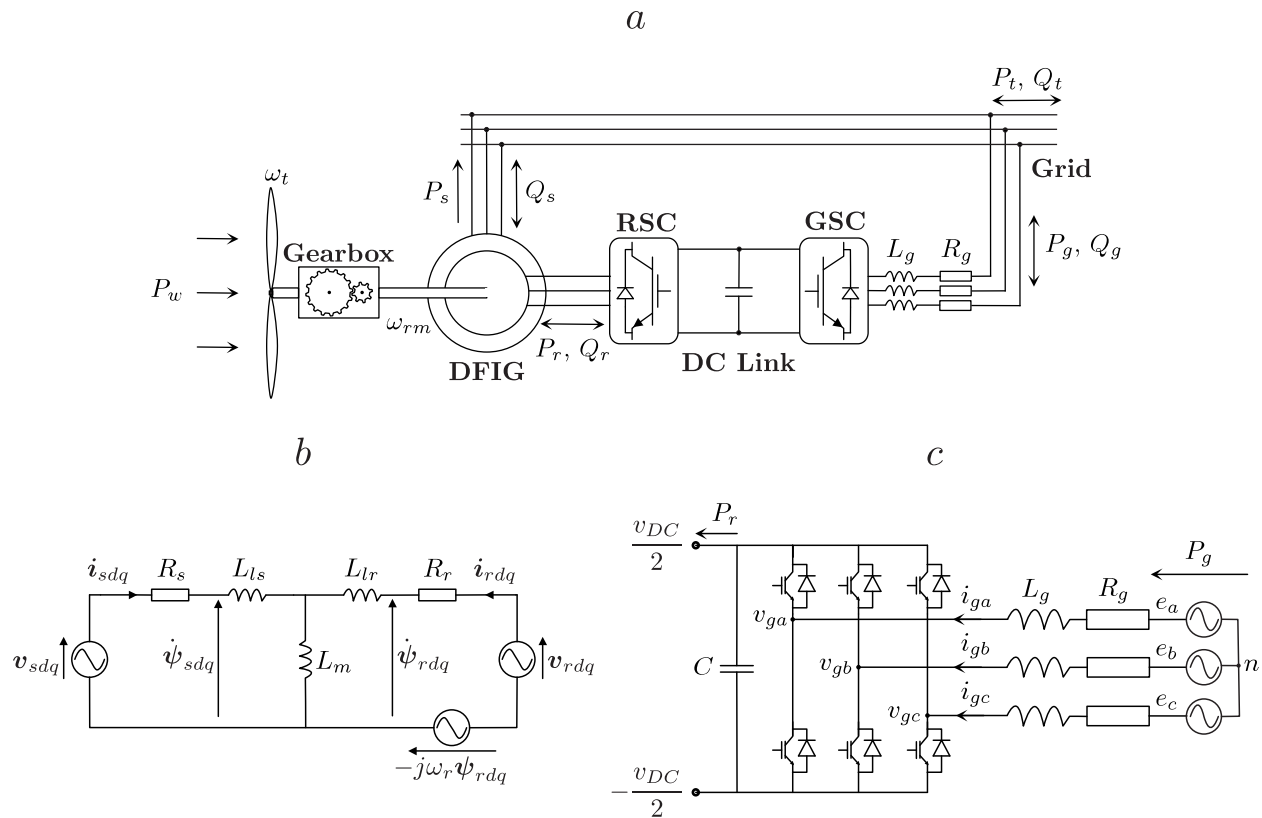
Fig. 1. *Structure of a DFIG-based wind turbine.* **a** *General scheme.* **b** *Equivalent circuit of a DFIG referred to the stationary reference frame.* **c** *Scheme of the grid-side power converter and the line filter.*

of the grid voltage —and also of currents, in the particular case of PI controllers—, and lack of robustness against parameter variations [11].

Likewise, robust solutions based on direct power control (DPC) and DPC+resonant (DPC+R) controllers were proposed in [12]–[15], having been devised to deal just with grid voltage imbalances. Although the problem of robustness against parameter deviations can be sorted out by applying those control proposals, voltage decomposition in sequences is still required in all cases except [12]. Besides, in DPC-based control strategies, it is usual to command the power converters with variable switching frequency, as in [13]–[15], therefore complicating the design of both the back-to-back power converter itself and the AC harmonic filter [16].

Several authors support the suitability of sliding-mode control (SMC)-based schemes for power electronics applications [11], [17], [18]. However, there exist different approaches to SMC, the following three being probably the most commonly adopted: 1) standard first-order SMC (S1-SMC) [18], [19], 2) non-standard first-order SMC (NS1-SMC) [16], [20], and 3) second-order SMC (2-SMC) [21], [22].

Even though all of them lead to robust closed-loop systems exhibiting high-performance dynamic responses, two are the main drawbacks jeopardising usefulness of the S1-SMC: namely, the variable switching frequency to which it leads and the chatter affecting control variables. Nevertheless, the NS1-SMC overcomes those problems by replacing the sign function with a smooth similar function such as the saturation or the sigmoid functions [23], hence giving rise to more than

acceptable results that might be comparable to those expected from a 2-SMC scheme.

In this context, aiming at covering the weaknesses that were so far identified regarding DFIG operation under non-ideal grid voltage conditions, the authors of this paper proposed a NS1-SMC-based solution in [20], which was only validated in simulation. The fact of designing the control algorithms in the stationary reference frame —rather than in rotary frames—, along with the non-linear nature of SMC, made possible to avoid decomposition in sequences or/and harmonic components of both the grid voltage and currents. Moreover, this solution led also to a constant switching frequency of the power converters, as well as to a high dynamic performance and robust control system against parameter uncertainties or variations.

Yet, as stated in [24], adoption of NS1-SMC causes the closed-loop system not to behave according to the sliding mode within the boundary layer, therefore seriously compromising the features inherent to sliding mode, as tracking accuracy, robustness and disturbance rejection. In contrast, the 2-SMC approach allows preventing that risk while preserving constant switching frequency [25]. Regarding tracking accuracy, it should be noted that, when it comes to distorted grid voltage scenarios, the ability of controllers to track rapidly varying reference values becomes crucial. The latter is due to the fact that, in most cases, avoiding the harmful effects caused by grid disturbances implies setting non-constant set-points —with frequencies even up to $6\omega_s$— for the control variables.

Bearing all above in mind, the present paper proposes two control algorithms —one for each power converter— based on 2-SMC. Both the design and tuning of the controllers follow the methodology described by the authors in [22]. The main contributions with respect to the control scheme put forward in [22] are both the fact that, apart from the RSC, the GSC is also addressed, and that the global control system is expressly designed in order to enable the wind turbine to simultaneously deal with grid voltage non-idealities of different nature.

The rest of this paper is organized as follows: Sections 3 and 4 tackle, respectively, control of the RSC and the GSC, addressing their respective mathematical models first and the design of their control algorithms later. Section 5 is focused on presenting the experimental results obtained when testing the 2-SMC algorithms detailed along the preceding sections on a 7-kW DFIG laboratory prototype. Finally, Section 6 draws the conclusions.

3. DFIG and rotor-side converter

3.1. Modelling

Fig. 1*b* shows the equivalent circuit of a DFIG, expressed in space-vector form according to the stationary reference frame. Adopting motor convention, its voltage equations are provided in [20] as

$$\boldsymbol{v}_{sdq} = R_s \boldsymbol{i}_{sdq} + \dot{\boldsymbol{\psi}}_{sdq} \tag{1}$$

$$\boldsymbol{v}_{rdq} = R_r \boldsymbol{i}_{rdq} + \dot{\boldsymbol{\psi}}_{rdq} - j\omega_r \boldsymbol{\psi}_{rdq}, \tag{2}$$

where

$$\boldsymbol{\psi}_{sdq} = L_s \boldsymbol{i}_{sdq} + L_m \boldsymbol{i}_{rdq} \tag{3}$$

$$\boldsymbol{\psi}_{rdq} = L_r \boldsymbol{i}_{rdq} + L_m \boldsymbol{i}_{sdq}. \tag{4}$$

Substitution of (3) and (4) into rotor voltage equation (2) allows identifying the dynamics of the rotor current direct- and quadrature-axis components as

$$\dot{i}_{rd} = \frac{v_{rd}}{L'_r} - \frac{R_r}{L'_r}i_{rd} - \frac{L_m}{L_sL'_r}\dot{\psi}_{sd} - \omega_r\left(i_{rq} + \frac{L_m}{L_sL'_r}\psi_{sq}\right) \tag{5}$$

$$\dot{i}_{rq} = \frac{v_{rq}}{L'_r} - \frac{R_r}{L'_r}i_{rq} - \frac{L_m}{L_sL'_r}\dot{\psi}_{sq} + \omega_r\left(i_{rd} + \frac{L_m}{L_sL'_r}\psi_{sd}\right), \tag{6}$$

where $L'_r = L_r - L_m^2/L_s$.

Both the electromagnetic torque and the stator reactive power are the control variables selected for the RSC sliding-mode controller, and they are estimated by means of the following expressions [20]:

$$T_e = \frac{3PL_m}{2L_s}\left|\boldsymbol{i}_{rdq} \times \boldsymbol{\psi}_{sdq}\right| = \frac{3PL_m}{2L_s}(i_{rd}\psi_{sq} - i_{rq}\psi_{sd}) \tag{7}$$

$$Q_s = \frac{3}{2}\left|\boldsymbol{i}_{sdq} \times \boldsymbol{v}_{sdq}\right| = \frac{3}{2}(v_{sq}i_{sd} - v_{sd}i_{sq}), \tag{8}$$

with '×' denoting cross product. In addition, the expression for Q_s given next, derived by replacing (3) into (8), is used not for control purposes, but for the design of the control algorithm:

$$\begin{aligned} Q_s &= \frac{3}{2L_s}\left|\boldsymbol{\psi}_{sdq} \times \boldsymbol{v}_{sdq}\right| + \frac{3L_m}{2L_s}\left|\boldsymbol{v}_{sdq} \times \boldsymbol{i}_{rdq}\right| = \\ &= \frac{3}{2L_s}(\psi_{sd}v_{sq} - \psi_{sq}v_{sd}) + \frac{3L_m}{2L_s}(v_{sd}i_{rq} - v_{sq}i_{rd}). \end{aligned} \tag{9}$$

The stator flux required to calculate the electromagnetic torque in (7) can be estimated, according to (1), as

$$\boldsymbol{\psi}_{sdq} = \int_0^t [\boldsymbol{v}_{sdq}(\tau) - R_s\boldsymbol{i}_{sdq}(\tau)]d\tau. \tag{10}$$

However, in practice, the integral operator is replaced by a band-pass filter (BPF) so as to avoid drift phenomenon. Furthermore, the BPF allows filtering the roughly static stator flux component —also referred to as natural flux [26]— which may arise when sudden stator voltage variations occur. As a consequence, the filter applied to estimate the stator flux, in which the stator resistive voltage-drop is neglected, may be represented via transfer function

$$\frac{\boldsymbol{\psi}_{sdq}(p)}{\boldsymbol{v}_{sdq}(p)} = \frac{p}{(p + \omega_0)^2}, \tag{11}$$

where p reflects the Laplace operator and ω_0 is the filter cut-off frequency.

It should be noticed that rotor current variations may cause the natural flux to slowly rotate. Consequently, excessively low values for ω_0 must be avoided in order to properly filter out the natural flux component. Thereby, such a flux component, as well as its effects —e.g. pulsating torques due to interaction with rotor current—, vanish on their own in approximately four times the stator time constant without the need for any specific control action.

3.2. 2-SMC of the RSC

Aiming at achieving satisfactory tracking performance for T_e and Q_s, the switching functions given next are adopted [20]:

$$s_{T_e} = \overbrace{T_e^* - T_e}^{e_{T_e}} + c_{T_e} \int_0^t e_{T_e}(\tau)d\tau \tag{12}$$

$$s_{Q_s} = \underbrace{Q_s^* - Q_s}_{e_{Q_s}} + c_{Q_s} \int_0^t e_{Q_s}(\tau)d\tau. \tag{13}$$

The integrals of the errors in (12) and (13), weighted by positive constants c_{T_e} and c_{Q_s}, cause the steady-state errors to be zero [27].

Taking the time derivatives of (12) and (13), and considering (5)–(7) and (9), the following dynamics arise for the selected switching functions:

$$\begin{bmatrix} \dot{s}_{T_e} \\ \dot{s}_{Q_s} \end{bmatrix} = \overbrace{\begin{bmatrix} F_{T_e} \\ F_{Q_s} \end{bmatrix}}^{\boldsymbol{F}_{T_e Q_s}} - r_c \overbrace{\begin{bmatrix} P\psi_{sq} & -P\psi_{sd} \\ -v_{sq} & v_{sd} \end{bmatrix}}^{\boldsymbol{R}} \begin{bmatrix} v_{rd} \\ v_{rq} \end{bmatrix}, \tag{14}$$

where

$$r_c = \frac{3}{2}K; \qquad K = \frac{L_m}{L_s L_r'}, \tag{15}$$

with

$$F_{T_e} = \dot{T}_e^* - \frac{3PL_m}{2L_s}\left[\dot{\psi}_{sq}i_{rd} - \dot{\psi}_{sd}i_{rq} - \psi_{sq}\overbrace{\left(\frac{R_r}{L_r'}i_{rd} + K\dot{\psi}_{sd} + \omega_r(i_{rq} + K\psi_{sq})\right)}^{X(t)} + \\ + \psi_{sd}\underbrace{\left(\frac{R_r}{L_r'}i_{rq} + K\dot{\psi}_{sq} - \omega_r(i_{rd} + K\psi_{sd})\right)}_{Y(t)}\right] + c_{T_e}e_{T_e} \tag{16}$$

$$F_{Q_s} = \dot{Q}_s^* + \frac{3L_m}{2L_s}\left[\dot{v}_{sq}i_{rd} - \dot{v}_{sd}i_{rq} - v_{sq}X(t) + v_{sd}Y(t)\right] + c_{Q_s}e_{Q_s} - \\ - \frac{3}{2L_s}\left(\dot{v}_{sq}\psi_{sd} - \dot{v}_{sd}\psi_{sq} + v_{sq}\dot{\psi}_{sd} - v_{sd}\dot{\psi}_{sq}\right). \tag{17}$$

The control signals in the stationary reference frame consist of the two following terms [25]:

- the super-twisting (ST) control term, $\boldsymbol{v}_{rdq_{ST}}$, aimed at providing a high performance dynamic response, disturbance rejection capability and robustness under structured and non-structured uncertainties, and

- the so-called equivalent control term, $\boldsymbol{v}_{rdq_{eq}}$, included in order to reduce the control effort to be done by the ST algorithm and to ease its tuning.

Thus,

$$
\overbrace{\begin{bmatrix} v_{rd} \\ v_{rq} \end{bmatrix}}^{\boldsymbol{v}_{rdq}} = \overbrace{\begin{bmatrix} v_{rd_{eq}} \\ v_{rq_{eq}} \end{bmatrix}}^{\boldsymbol{v}_{rdq_{eq}}} + \overbrace{\begin{bmatrix} v_{rd_{ST}} \\ v_{rq_{ST}} \end{bmatrix}}^{\boldsymbol{v}_{rdq_{ST}}}.
\tag{18}
$$

Equivalent control can be straightforwardly calculated by forcing $\dot{s}_{T_e}$ and $\dot{s}_{Q_s}$ in (14) to zero and solving for v_{rd} and v_{rq} [18]. The latter results in

$$
\boldsymbol{v}_{rdq_{eq}} = \frac{\boldsymbol{R}^{-1}}{r_c} \boldsymbol{F}_{T_e Q_s} = \frac{1}{r_c P \underbrace{(\psi_{sq} v_{sd} - \psi_{sd} v_{sq})}_{|\boldsymbol{v}_{sdq} \times \boldsymbol{\psi}_{sdq}|}} \begin{bmatrix} v_{sd} & P\psi_{sd} \\ v_{sq} & P\psi_{sq} \end{bmatrix} \boldsymbol{F}_{T_e Q_s}.
\tag{19}
$$

From (11), it follows that $\boldsymbol{v}_{sdq}$ is practically in quadrature with $\boldsymbol{\psi}_{sdq}$, therefore implying that $\left|\boldsymbol{v}_{sdq} \times \boldsymbol{\psi}_{sdq}\right| \neq 0$ and that, in turn, matrix $\boldsymbol{R}$ is invertible. It is also worth mentioning that Euler's forward rectangular method is applied to compute the time derivatives that, by virtue of (16) and (17), are present in $\boldsymbol{F}_{T_e Q_s}$.

Although analysis of (15)–(17) evidences that the equivalent control in (19) turns out being highly parameter dependent, robustness of the overall control algorithm in (18) is not compromised, as it does actually lie on the following ST control terms:

$$
\boldsymbol{v}_{rdq_{ST}} = \frac{\boldsymbol{R}^{-1}}{r_c} \boldsymbol{v}_{T_e Q_{sST}} = \frac{1}{r_c P (\psi_{sq} v_{sd} - \psi_{sd} v_{sq})} \begin{bmatrix} v_{sd} & P\psi_{sd} \\ v_{sq} & P\psi_{sq} \end{bmatrix} \boldsymbol{v}_{T_e Q_{sST}},
\tag{20}
$$

where $\boldsymbol{v}_{T_e Q_{sST}}$ is calculated by applying the ST algorithm by Levant [28] as

$$
\boldsymbol{v}_{T_e Q_{sST}} = \begin{bmatrix} v_{T_{eST}} \\ v_{Q_{sST}} \end{bmatrix} = \begin{bmatrix} \lambda_{T_e} \sqrt{|s_{T_e}|} \operatorname{sgn}(s_{T_e}) + w_{T_e} \int_0^t \operatorname{sgn}(s_{T_e}(\tau)) \, d\tau \\ \lambda_{Q_s} \sqrt{|s_{Q_s}|} \operatorname{sgn}(s_{Q_s}) + w_{Q_s} \int_0^t \operatorname{sgn}(s_{Q_s}(\tau)) \, d\tau \end{bmatrix},
\tag{21}
$$

with the first addends of $v_{T_{eST}}$ and $v_{Q_{sST}}$ being responsible for guaranteeing that switching surfaces $s_{T_e} = 0$ and $s_{Q_s} = 0$ are reached in finite time.

As a result, six are the parameters to be adjusted: c_{T_e}, c_{Q_s}, λ_{T_e}, w_{T_e}, λ_{Q_s} and w_{Q_s}, which must all be strictly positive constants. To that end, the approach detailed by the authors in [22] is followed. In particular, application of the tuning methodology presented in [22] imples that, while in sliding regime, the dynamics of the controlled variable error, e_x, may be roughly represented by the third-order characteristic equation given next:

$$
\left(p^2 + 2\xi_x \omega_{nx} p + \omega_{nx}^2\right)(p + \alpha \xi_x \omega_{nx}) = 0,
\tag{22}
$$

where subscript 'x' denotes either 'T_e' or 'Q_s'.

By selecting α high enough —typically, $\alpha \geq 10$—, the second-order term of the characteristic polynomial in the left-hand side of (22) becomes dominant, therefore causing e_x to show approximately a ξ_x damping coefficient and a ω_{nx} natural frequency while it vanishes to zero.

In addition to α, ξ_x and ω_{nx}, the designer should specify a strictly positive value for parameter δ_x, which, in broad terms, may be interpreted as the absolute value of the maximum admissible deviation of switching variable s_x from zero. Accordingly, application of the methodolody in [22] leads to the tuning equations given next:

$$
c_{T_e}^3 - (2 + \alpha)\, \xi_{T_e} \omega_{nT_e} c_{T_e}^2 + \left(1 + 2\alpha \xi_{T_e}^2\right) \omega_{nT_e}^2 c_{T_e} - \alpha \xi_{T_e} \omega_{nT_e}^3 = 0
\tag{23}
$$

$$c_{Q_s}^3 - (2+\alpha)\,\xi_{Q_s}\omega_{nQ_s}c_{Q_s}^2 + \left(1 + 2\alpha\xi_{Q_s}^2\right)\omega_{nQ_s}^2 c_{Q_s} - \alpha\xi_{Q_s}\omega_{nQ_s}^3 = 0 \tag{24}$$

$$\lambda_{T_e} = 2\sqrt{\delta_{T_e}}\left[(2+\alpha)\,\xi_{T_e}\omega_{nT_e} - c_{T_e}\right] \tag{25}$$

$$w_{T_e} = \frac{\delta_{T_e}\alpha\xi_{T_e}\omega_{nT_e}^3}{c_{T_e}} \tag{26}$$

$$\lambda_{Q_s} = 2\sqrt{\delta_{Q_s}}\left[(2+\alpha)\,\xi_{Q_s}\omega_{nQ_s} - c_{Q_s}\right] \tag{27}$$

$$w_{Q_s} = \frac{\delta_{Q_s}\alpha\xi_{Q_s}\omega_{nQ_s}^3}{c_{Q_s}}. \tag{28}$$

As reasoned in [22], it is guaranteed that at least one of the three solutions for c_{T_e} and c_{Q_s} will be both real and positive, as required. If (23) and (24) give rise to more than one feasible solution for, respectively, c_{T_e} and c_{Q_s}, the lowest ones lead generally to better performance.

   Implementation of the 2-SMC algorithm for the RSC is accomplished as displayed in the left-hand column of the functional diagram in Fig. 2, which is built by assuming that any variable present in a given layer of the diagram is also available to all the layers inside. Accordingly, the 2-SMC algorithm should be implemented from the outer to the inner layer —labelled as '1st Step' and '3rd Step' at their respective bottoms.

4.   Grid-side converter

4.1.   Modelling

Adopting the rectifier convention and neglecting losses in both the power converter and the line filter, the dynamics of DC-link voltage may be represented by

$$\dot{v}_{DC} = \frac{P_g - P_r}{Cv_{DC}}, \tag{29}$$

with

$$P_g = \frac{3}{2}(e_{dn}i_{gd} + e_{qn}i_{gq}) \tag{30}$$

$$Q_g = \frac{3}{2}(e_{qn}i_{gd} - e_{dn}i_{gq}) \tag{31}$$

when expressed in the stationary reference frame.

   Accordingly, based on Fig. 1c, the electrical equations describing the behaviour of the GSC are given in [12] as

$$\dot{i}_{gd} = \frac{1}{L_g}(e_{dn} - v_{gd} - R_g i_{gd}) \tag{32}$$

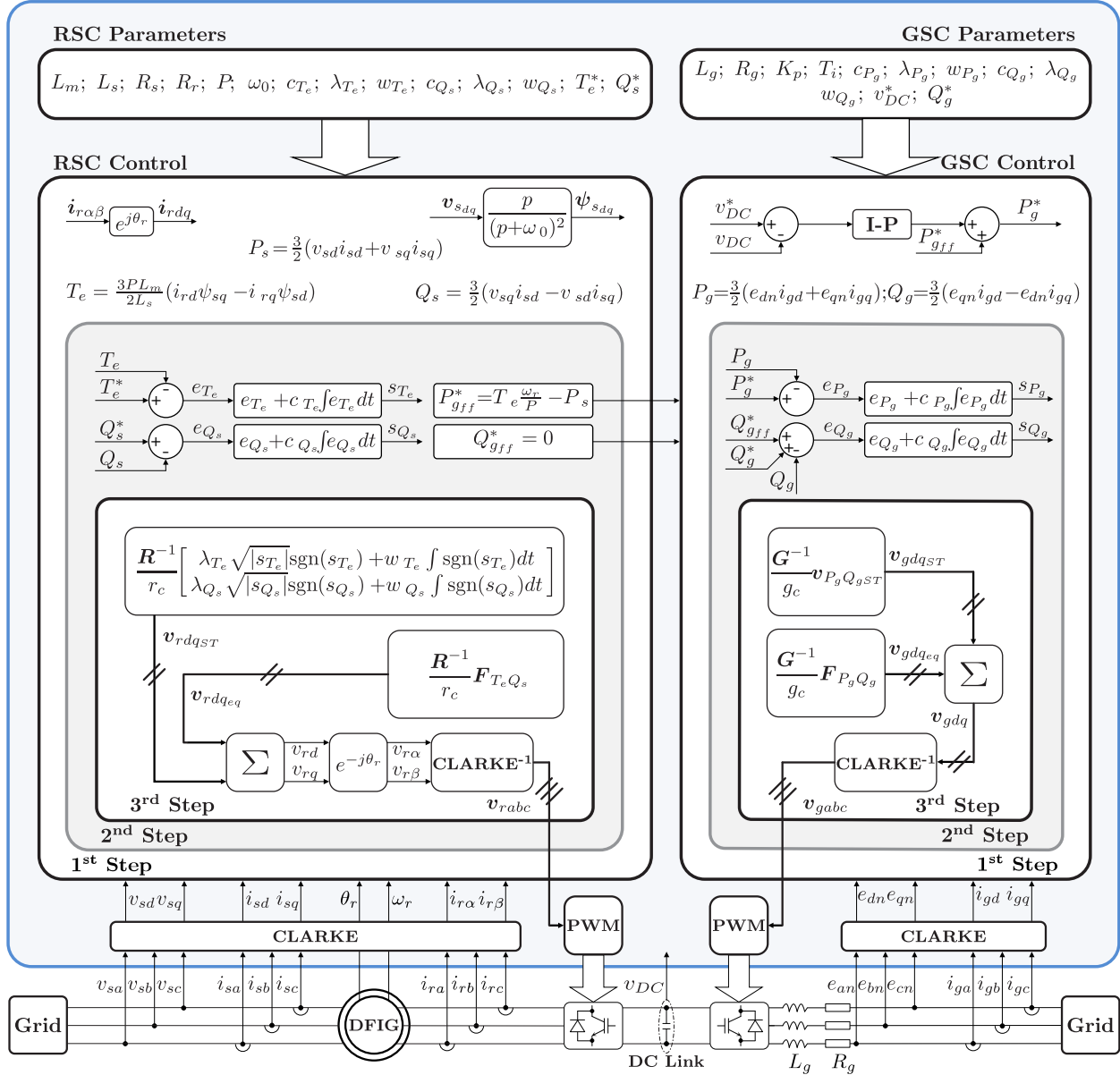$$\dot{i}_{gq} = \frac{1}{L_g}(e_{qn} - v_{gq} - R_g i_{gq}). \tag{33}$$

Fig. 2. *Functional diagram of the proposed global control scheme for the DFIG.*

4.2. GSC control system

The right-hand column of the functional diagram in Fig. 2 displays the overall GSC control algorithm. In order to keep the DC-link voltage at its set-point value, an integral-proportional (I-P) controller is cascaded to the P_g control loop of the 2-SMC scheme governing both P_g and Q_g. The GSC control system can additionally satisfy further control targets of interest [13]. For that purpose, appropriate values for $P^*_{g_{ff}}$ and $Q^*_{g_{ff}}$ feedforward compensation terms —refer to Fig. 2— need to be established.

If getting the lowest possible output current total harmonic distortion (THD) is desirable, then adequate expressions for $P^*_{g_{ff}}$ and $Q^*_{g_{ff}}$ are those derived by the authors in [20], and should be

computed as

$$P^*_{g_{ff}} = -\frac{3}{2}\left(e_{dn}i_{sd_h} + e_{qn}i_{sq_h}\right) \tag{34}$$

$$Q^*_{g_{ff}} = -\frac{3}{2}\left(e_{qn}i_{sd_h} - e_{dn}i_{sq_h}\right), \tag{35}$$

where i_{sd_h} and i_{sq_h} may be estimated by notch-filtering out the 50-Hz fundamental frequency from, respectively, stator current i_{sd} and i_{sq} components. Such a strategy will however give rise to DC-link voltage fluctuations during grid disturbances, as well as to oscillations in total active and reactive powers.

In this paper, the following expressions are defined for $P^*_{g_{ff}}$ and $Q^*_{g_{ff}}$ signals:

$$P^*_{g_{ff}} = T_e\omega_{rm} - P_s \tag{36}$$

$$Q^*_{g_{ff}} = 0, \tag{37}$$

with

$$P_s = \frac{3}{2}\left(v_{sd}i_{sd} + v_{sq}i_{sq}\right) \tag{38}$$

and T_e being computed according to (7). This way, practically no DC-link voltage oscillations arise under non-ideal grid voltages, and total active and reactive powers remain free of fluctuations, although, in return, the THD of the overall current injected into the grid turns out to be higher [19].

Regarding DC-link voltage I-P controller tuning, dynamic model (29) is firstly linearised around the rated value of the DC-link voltage, v_{DC0}. Based on such linearised model, subsequent application of the pole placement technique allows defining the following tuning formulas for the I-P proportional gain and integral time constant:

$$K_p = 2\xi_{DC}\omega_{nDC}Cv_{DC0} \tag{39}$$

$$T_i = \frac{2\xi_{DC}}{\omega_{nDC}}, \tag{40}$$

where ξ_{DC} and ω_{nDC} represent, respectively, the target damping coefficient and natural frequency for the DC-link voltage control-loop, being both parameters directly related to the settling time and overshoot of the latter's closed-loop response.

4.2.1. 2-SMC of the GSC: The goal of the GSC sliding-mode controller consists in governing the active and reactive powers interchanged with the grid —P_g and Q_g—, and it is designed by adopting the same approach as in Section 3.2, based on the following switching functions:

$$s_{P_g} = \overbrace{P^*_g - P_g}^{e_{P_g}} + c_{P_g}\int_0^t e_{P_g}(\tau)d\tau \tag{41}$$

$$s_{Q_g} = \underbrace{Q^*_g - Q_g}_{e_{Q_g}} + c_{Q_g}\int_0^t e_{Q_g}(\tau)d\tau. \tag{42}$$

Making use of (30)–(33), the dynamics of the preceding switching variables may be derived as

$$\begin{bmatrix} \dot{s}_{P_g} \\ \dot{s}_{Q_g} \end{bmatrix} = \overbrace{\begin{bmatrix} F_{P_g} \\ F_{Q_g} \end{bmatrix}}^{\boldsymbol{F}_{P_gQ_g}} - g_c \overbrace{\begin{bmatrix} -e_{dn} & -e_{qn} \\ -e_{qn} & e_{dn} \end{bmatrix}}^{\boldsymbol{G}} \begin{bmatrix} v_{gd} \\ v_{gq} \end{bmatrix}, \tag{43}$$

with

$$F_{P_g} = \dot{P}_g^* - \frac{3}{2}\left(\dot{e}_{dn}i_{gd} + \dot{e}_{qn}i_{gq}\right) - \frac{3}{2L_g}\left(e_{dn}^2 + e_{qn}^2\right) + \frac{R_g}{L_g}P_g + c_{P_g}e_{P_g} \tag{44}$$

$$F_{Q_g} = \dot{Q}_g^* - \frac{3}{2}\left(\dot{e}_{qn}i_{gd} - \dot{e}_{dn}i_{gq}\right) + \frac{R_g}{L_g}Q_g + c_{Q_g}e_{Q_g} \tag{45}$$

$$g_c = \frac{3}{2L_g}. \tag{46}$$

Following the same modus operandi as that adopted for the design of the RSC control algorithm, the control signals for the GSC —also referred to the stationary reference frame— are computed as

$$\overbrace{\begin{bmatrix} v_{gd} \\ v_{gq} \end{bmatrix}}^{\boldsymbol{v}_{gdq}} = \overbrace{\begin{bmatrix} v_{gd_{eq}} \\ v_{gq_{eq}} \end{bmatrix}}^{\boldsymbol{v}_{gdq_{eq}}} + \overbrace{\begin{bmatrix} v_{gd_{ST}} \\ v_{gq_{ST}} \end{bmatrix}}^{\boldsymbol{v}_{gdq_{ST}}}, \tag{47}$$

where

$$\boldsymbol{v}_{gdq_{eq}} = \frac{\boldsymbol{G}^{-1}}{g_c}\boldsymbol{F}_{P_gQ_g} = \frac{1}{g_c\underbrace{\left(e_{dn}^2 + e_{qn}^2\right)}_{|e_n|^2}}\begin{bmatrix} -e_{dn} & -e_{qn} \\ -e_{qn} & e_{dn} \end{bmatrix}\boldsymbol{F}_{P_gQ_g}, \tag{48}$$

with matrix $\boldsymbol{G}$ being evidently invertible, and

$$\boldsymbol{v}_{gdq_{ST}} = \frac{\boldsymbol{G}^{-1}}{g_c}\boldsymbol{v}_{P_gQ_{gST}} = \frac{1}{g_c\left(e_{dn}^2 + e_{qn}^2\right)}\begin{bmatrix} -e_{dn} & -e_{qn} \\ -e_{qn} & e_{dn} \end{bmatrix}\boldsymbol{v}_{P_gQ_{gST}}, \tag{49}$$

where $\boldsymbol{v}_{P_gQ_{gST}}$ is given by

$$\boldsymbol{v}_{P_gQ_{gST}} = \begin{bmatrix} v_{P_{gST}} \\ v_{Q_{gST}} \end{bmatrix} = \begin{bmatrix} \lambda_{P_g}\sqrt{|s_{P_g}|}\,\mathrm{sgn}\left(s_{P_g}\right) + w_{P_g}\int_0^t \mathrm{sgn}\left(s_{P_g}(\tau)\right)d\tau \\ \lambda_{Q_g}\sqrt{|s_{Q_g}|}\,\mathrm{sgn}\left(s_{Q_g}\right) + w_{Q_g}\int_0^t \mathrm{sgn}\left(s_{Q_g}(\tau)\right)d\tau \end{bmatrix}. \tag{50}$$

Similarly to the case of the RSC control algorithm, c_{P_g}, c_{Q_g}, λ_{P_g}, w_{P_g}, λ_{Q_g} and w_{Q_g} in (41), (42) and (50) are positive constants to be tuned. As a result of the analogy existing between the RSC control signals in (18)–(21) and those of the GSC in (47)–(50), tuning equations (23)–(28) turn out to be also valid for the GSC control scheme after replacing subscripts 'T_e' and 'Q_s' by, respectively, 'P_g' and 'Q_g'. Accordingly, if α is selected to be equal to 10, it turns out that

$$c_{P_g}^3 - 12\xi_{P_g}\omega_{nP_g}c_{P_g}^2 + \left(1 + 20\xi_{P_g}^2\right)\omega_{nP_g}^2 c_{P_g} - 10\xi_{P_g}\omega_{nP_g}^3 = 0 \tag{51}$$

$$c_{Q_g}^3 - 12\xi_{Q_g}\omega_{nQ_g}c_{Q_g}^2 + \left(1 + 20\xi_{Q_g}^2\right)\omega_{nQ_g}^2 c_{Q_g} - 10\xi_{Q_g}\omega_{nQ_g}^3 = 0 \tag{52}$$

$$\lambda_{P_g} = 2\sqrt{\delta_{P_g}} \left(12\xi_{P_g}\omega_{nP_g} - c_{P_g} \right) \tag{53}$$

$$w_{P_g} = \frac{10\delta_{P_g}\xi_{P_g}\omega_{nP_g}^3}{c_{P_g}} \tag{54}$$

$$\lambda_{Q_g} = 2\sqrt{\delta_{Q_g}} \left(12\xi_{Q_g}\omega_{nQ_g} - c_{Q_g} \right) \tag{55}$$

$$w_{Q_g} = \frac{10\delta_{Q_g}\xi_{Q_g}\omega_{nQ_g}^3}{c_{Q_g}}. \tag{56}$$

Finally, it should be pointed out that, aiming at avoiding generation of noisy control signals, $\dot{P}_g^* = 0$ may be assumed in (44) without affecting the GSC control system performance [20]. The remaining time derivatives in (44) and (45), required to compute the equivalent control term in (48), are again estimated through application of Euler's forward rectangular method.

Regarding implementation of the GSC control algorithm, it is carried out by following the right-hand column of the functional diagram in Fig. 2.

5. Experimental validation

Experimental validation of the global control scheme presented throughout Sections 3.2 and 4.2 was carried out on the 7-kW DFIG test bench shown in Fig. 3*b*. The electrical parameters of the DFIG under consideration are collected in Table 1. As sketched in Fig. 3*a*, the DFIG is driven by a 15-kW armature-controlled DC motor, whose rotational speed can be commanded by means of a commercial adjustable speed drive. The OP5600 platform by Opal-RT was used to perform rapid control prototyping (RCP) of both the RSC and GSC control schemes.

On the other hand, it was observed that a significant degree of harmonic distortion, as well as a slight one-phase imbalance, are inherent to the grid voltage of the laboratory in which the experimental setup is installed. However, in order to keep direct control of imbalances, a device similar to that described in [29] was developed —refer to Figs. 3*a* and *c*—, which allows reproducing controlled two-phase imbalances of type E [30].

The value of ω_0 in (11) was selected to be $\omega_0 = 1.2\pi$ rad/s. Regarding the DC-link voltage I-P controller, $\xi_{DC} = 1$ and $\omega_{nDC} = 19.3333$ rad/s were set in (39) and (40), which corresponds to demanding a closed-loop response for v_{DC} showing no overshoot and a 300-ms settling time. Accordingly, $K_p = 45.4333$ W/V and $T_i = 103.4483$ ms.

Control parameters for the 2-SMC algorithms were computed according to tuning equations (23)–(28) and (51)–(56). The specifications required to apply those tuning formulas, along with the resulting control parameter values, are collected in Table 2.

Finally, the sample time of the two control algorithms was fixed to be $50~\mu$s, and a switching frequency of 10 kHz was adopted for both the RSC and GSC.

This section is divided into two parts. Performance of the proposed overall 2-SMC scheme under a realistic rotational speed profile for a wind turbine-driven DFIG and different grid voltage conditions is evaluated in Section 5.1, whereas Section 5.2 assesses robustness of both the RSC and GSC control algorithms against simultaneous disturbances and electrical parameter deviations.
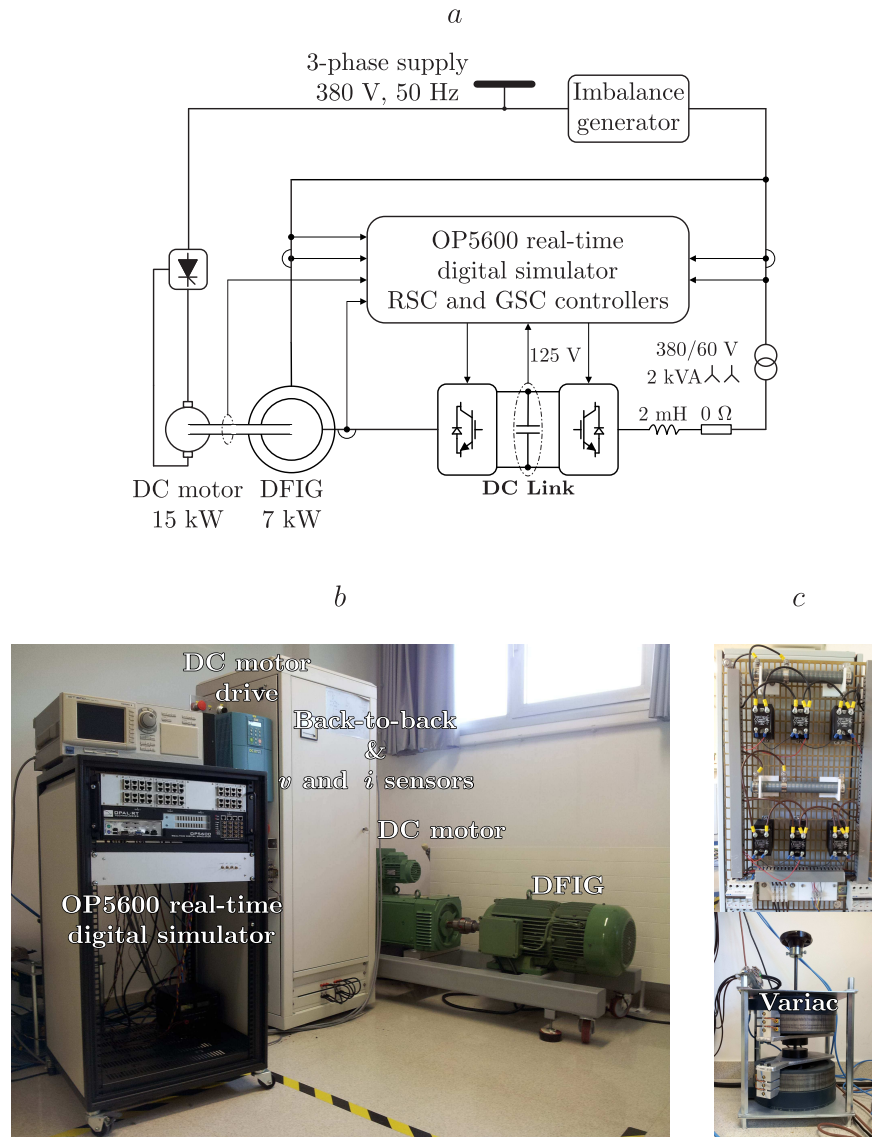
a

b   *c*

Fig. 3. *Experimental setup.* **a** *Connection diagram.* **b** *General view of the test bench.* **c** *Equipment reproducing controlled two-phase voltage imbalances.*

5.1. Performance of the global 2-SMC scheme

It is desirable to evaluate the proposed control system under a deep imbalance. In this sense, according to different countries' grid codes [31], severe imbalances correspond to voltage drops of around 15% of their nominal value. Thereby, the grid voltage upon which the system was tested is displayed in Figs. 4*a*, *b* and *c*, evidencing the presence of a two-phase imbalance of a roughly 15% depth between seconds 5 and 31. A substantial harmonic distortion was also present all through the test, as suggested by the trapezoid-like waveforms in Fig. 4*c*.

   The well-known maximum power point tracking (MPPT) strategy was adopted. Accordingly, the reference value for the electromagnetic torque was set by the speed-dependent quadratic expression given next:

$$T_e^* = aw_{rm}^2 + bw_{rm} + c, \tag{57}$$

Table 1 7-kW DFIG electrical parameters

Parameter	Value
$\|\boldsymbol{v}_s\|, \|\boldsymbol{e}_{n1}\|$	$380\sqrt{2/3}$ V
R_s, L_{ls}	370 mΩ, 4.86 mH
R_r, L_{lr}	145.8541 mΩ, 1.2138 mH
L_m	37.6812 mH
n	2.001
$L_s = L_{ls} + nL_m$	80.2601 mH
$L_r = L_{lr} + L_m/n$	20.045 mH
P	2
v_{DC0}	125 V
C	9.4 mF
R_g, L_g	0 mΩ, 2 mH

Table 2 Specifications for the 2-SMC tuning equations and resulting control parameters

	Specification	Value	Parameter	Value
RSC	ξ_{T_e}, ξ_{Q_s}	1	c_{T_e}, c_{Q_s}	3.8667×10^3 s^{-1}
	$\omega_{nT_e}, \omega_{nQ_s}$	3.8667×10^3 rad/s	λ_{T_e}	1.9197×10^3 (Nm)$^{0.5}$/s
	δ_{Q_s}	80×10^{-3} VAr	λ_{Q_s}	24.0605×10^3 VAr$^{0.5}$/s
	δ_{T_e}	$\delta_{Q_s}/(\omega_s/P) = 509.2958\times10^{-6}$ Nm	w_{T_e}	76.1454×10^3 Nm
	α	10	w_{Q_s}	11.9609×10^6 VAr
GSC	ξ_{P_g}, ξ_{Q_g}	1	c_{P_g}, c_{Q_g}	96.6667 s^{-1}
	$\omega_{nP_g}, \omega_{nQ_g}$	96.6667 rad/s	λ_{P_g}	33.6256×10^3 W$^{0.5}$/s
	δ_{P_g}	250 W	λ_{Q_g}	10.6333×10^3 VAr$^{0.5}$/s
	δ_{Q_g}	25 VAr	w_{P_g}	23.3611×10^6 W
	α	10	w_{Q_g}	2.3361×10^6 VAr

where parameters a, b and c depend exclusively on the specific shape of the wind turbine. During experimentation, they were assumed to be $a = -4.6015 \times 10^{-5}$ Nm/(rpm)^2, $b = 8.0144 \times 10^{-2}$ Nm/rpm and $c = -43.8997$ Nm, while the actual DFIG rotational speed and its corresponding reference —fed into the DC motor drive— were those depicted in Fig. 4d. Such a reference speed profile was previously obtained off-line, as a result of feeding with real wind speed data the simulation model of a 2-MW wind turbine. The drive-train of the latter was represented by means of a two-mass model, whose per unit mechanical parameters were taken from [32]. Beyond assessing its robustness against parametric and modelling uncertainties, this approach allowed also testing robustness of the global 2-SMC strategy against disturbances attributable to wind variability.

Finally, a unity power factor was requested to the entire generating unit, so that $Q_s^* = Q_g^* = 0$.

The electromagnetic torque and stator reactive power, together with their associated reference values, are reflected, respectively, in Figs. 5a and b. Satisfactory tracking of T_e^* is achieved. In addition, although a certain amount of chatter affects both variables, it is considered acceptable.
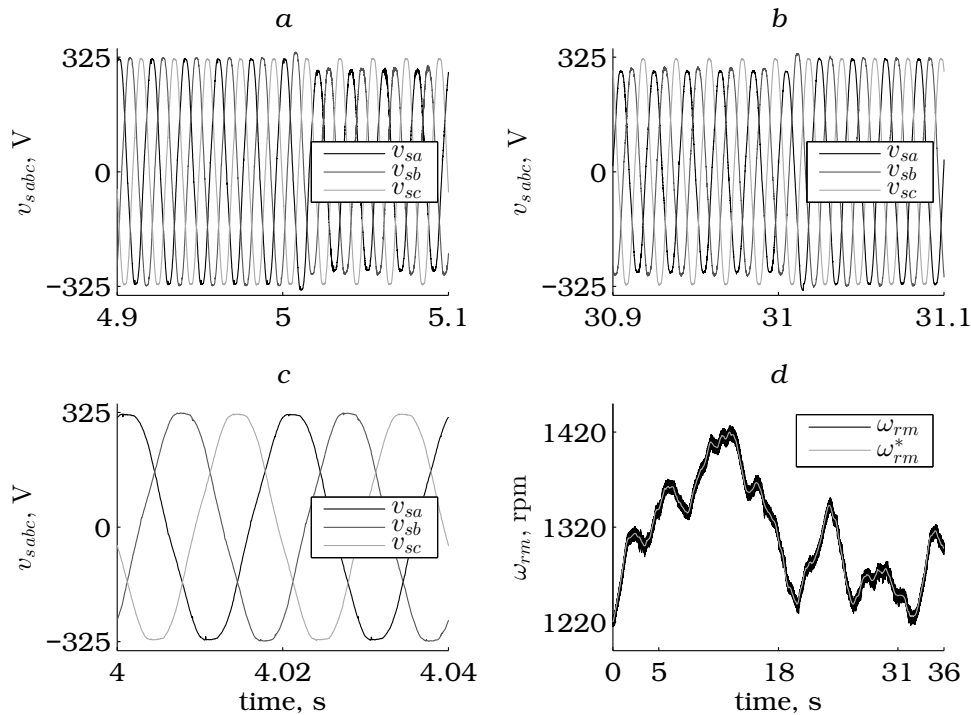
Fig. 4. *Grid voltage and rotational speed signals. **a** Zoom of the grid voltage at the initial instant of the imbalance. **b** Zoom of the grid voltage at the final instant of the imbalance. **c** Zoom of the distorted laboratory grid voltage in normal operating conditions. **d** Rotational speed of the DFIG and speed reference provided to the DC motor drive.*

Specifically, torque chatter turns out being lower than $\pm 1.5\%$ of its rated value, while a roughly $\pm 1\%$ chatter is present in the stator reactive power.

Nevertheless, the main inconvenient that a disturbed grid voltage may provoke is the appearance of oscillations affecting the electromagnetic torque and the stator active and reactive powers, which, in addition, may be of different frequencies depending on the specific grid voltage disturbance —e.g. of 100 Hz in the case of an imbalance, and of 300 Hz in the presence of 5th and 7th order harmonics. Such oscillations arise owing to the interaction among voltage and current space vectors of different natures —or angular frequencies—, being the magnitude of fluctuations dependent not only on the disturbance severity but also on the amount of power that is being generated —at higher powers, higher pulsations [33].

Yet, analysis of Figs. 5*a* and *b* reveals that neither the electromagnetic torque nor the stator reactive power fluctuate. This is due to the fact that those were precisely the signals selected to be the control variables of the RSC control algorithm. Consequently, oscillations only affect the stator active power, as evidenced in Fig. 5*c*. However, in accordance with (36), such undesired fluctuations can be mitigated by injecting the same amount of oscillating active power, though in opposition, from the GSC. As a result, fluctuations in the total active power are practically removed, as illustrated by Fig. 5*d*.

When the grid voltage happens to be unbalanced, negative sequence components arise in both the stator and rotor currents, thus leading to an unbalanced stator current on the one hand, and to a distorted rotor current —with harmonics of frequency $f_s + f_r$— on the other hand, as observable,
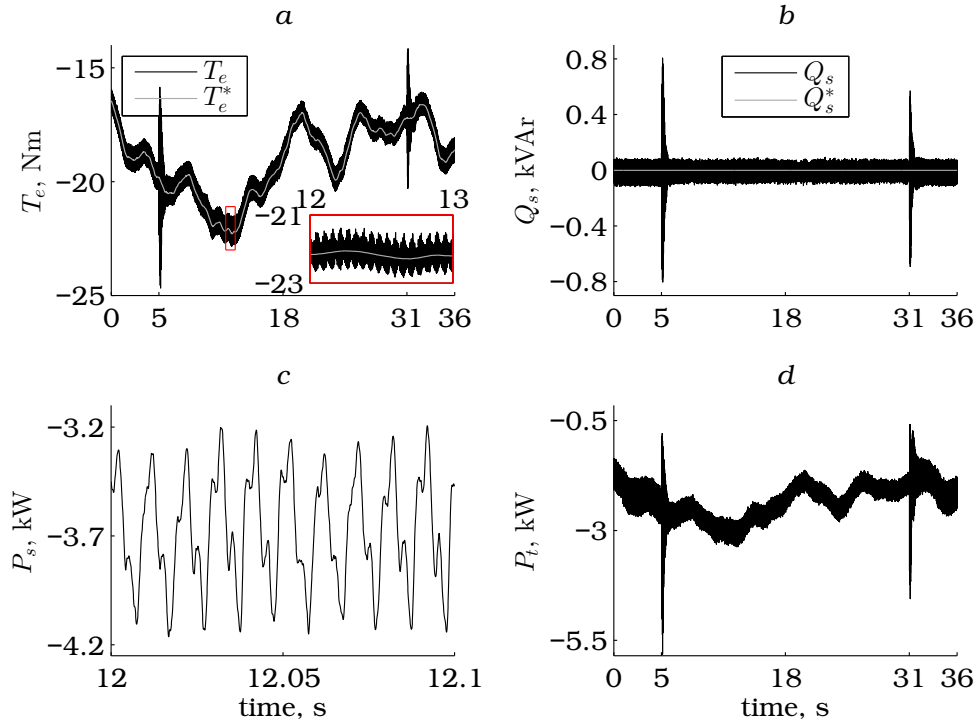
Fig. 5. *Variables related to the RSC control system.* **a** *Electromagnetic torque.* **b** *Stator reactive power.* **c** *Zoom of the stator active power during the imbalance.* **d** *Total active power.*

respectively, in Figs. 6*a* and *b*. Similarly, the inherent harmonic distortion of the laboratory grid voltage causes additional space vectors to be incorporated to the stator and rotor currents, which are translated into harmonics within their respective three-phase signals. While the stator current harmonics are of the same order as those in the grid voltage, the harmonics in the rotor current behave differently due to its natural reference frame being rotary. Thereby, a given grid voltage harmonic of order h produces rotor current harmonics whose frequency turns out being $hf_s + f_r$ or $hf_s - f_r$, depending on whether h corresponds, respectively, to the negative —e.g. 5th order— or positive —e.g. 7th order— sequence.

Regarding the most significant signals related to the GSC control system, Fig. 7*a* displays the DC-link voltage, which was regulated by the I-P controller to remain at 125 V. On the other hand, the grid-side active and reactive powers controlled by the 2-SMC algorithm are respectively shown in Figs. 7*b* and *c*. As previously mentioned, in order to compensate for the active power oscillations injected from the stator in the presence of a disturbed grid voltage, the grid-side active power should be pulsating. In this context, Fig. 7*d* clearly evidences the tracking capability conferred by 2-SMC. In return, as a result of the fluctuating grid-side active power, the current at the grid-side is no longer purely sinusoidal, as reflected in Fig. 6*c*.

It is important to remark that, due to the distorted grid-side current, the THD of the total current injected into the grid by the overall generating unit, which results from adding the stator and grid-side three-phase currents —refer to Fig. 6*d*—, may exceed the THD limit recommended by the standards. In such a case, an alternative strategy for setting the feedforward $P_{g_{ff}}^*$ and $Q_{g_{ff}}^*$ compensation terms might be applied, as suggested at the beginning of Section 4.2.

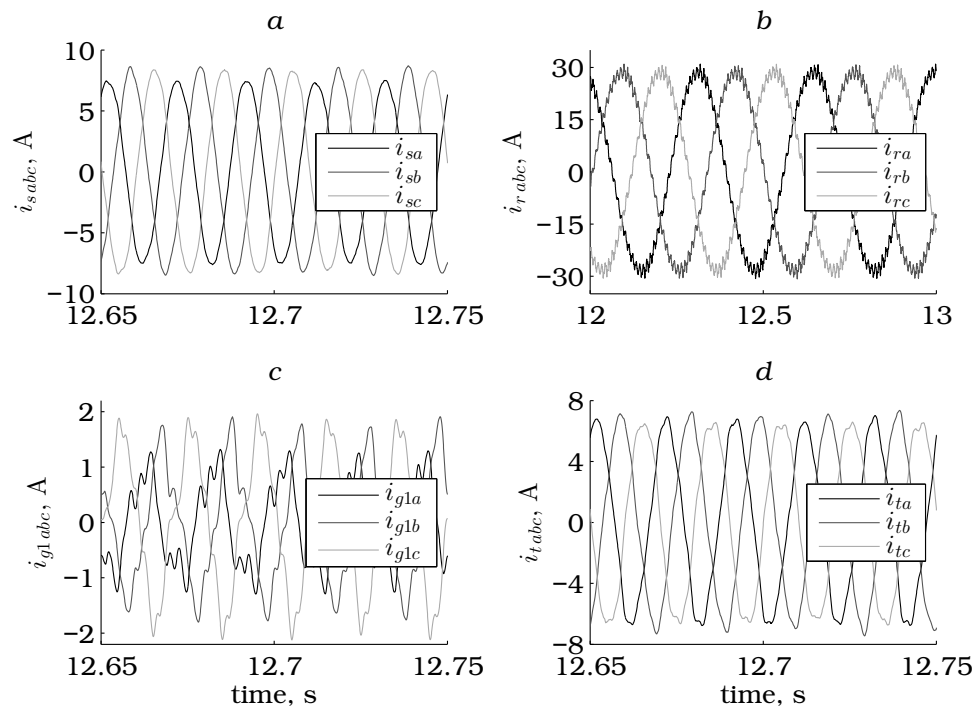For the strategy adopted in this paper, the total current presents a 3.9%, 1.51% and 2.44% of the

Fig. 6. *Zooms of three-phase currents during the imbalance.* **a** *Stator current.* **b** *Rotor current.*
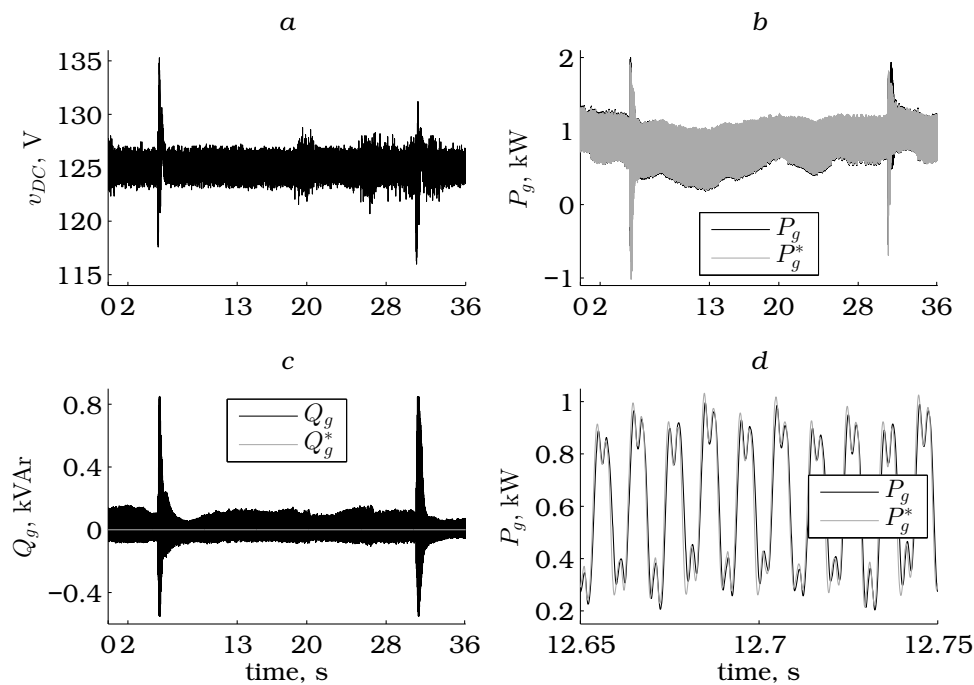**c** *Grid-side current at the primary of the transformer.* **d** *Total current.*

Fig. 7. *Variables related to the GSC control system.* **a** *DC-link voltage.* **b** *Grid-side active power.*
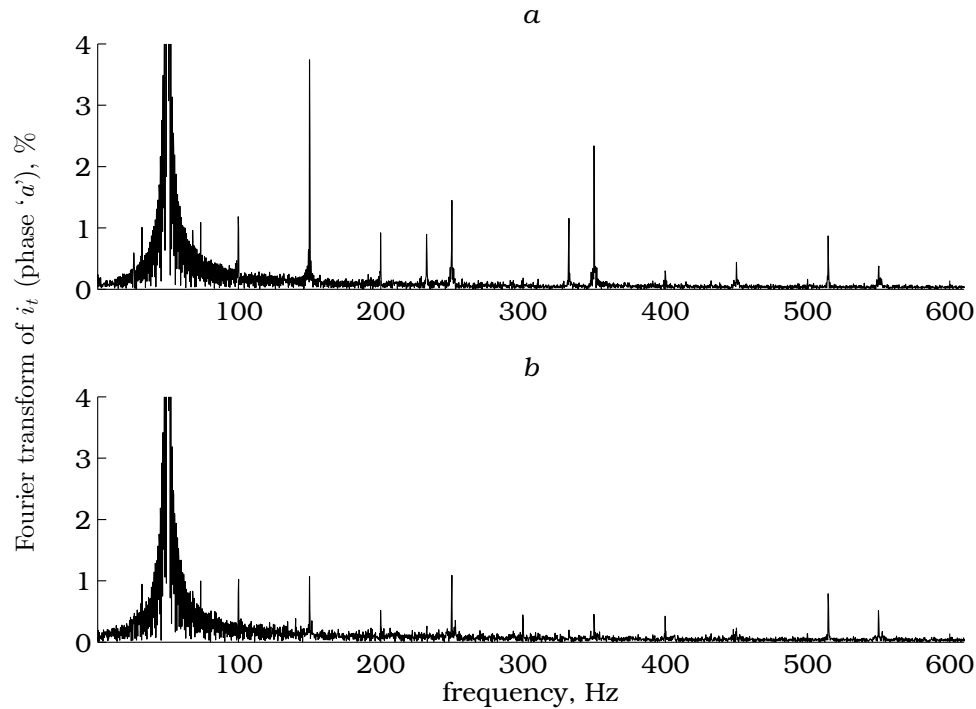**c** *Grid-side reactive power.* **d** *Zoom of the grid-side active power during the imbalance.*

Fig. 8. *Frequency spectrum of the total current —phase 'a'— injected into the grid.* ***a*** *Strategy adopted in this paper.* ***b*** *Strategy proposed in [20].*

3rd, 5th and 7th order harmonics, respectively, as evidenced in the frequency spectrum displayed in Fig. 8a. However, if required, those percentages may be considerably reduced by applying the strategy proposed by the authors in [20], hence fixing $P^*_{g_{ff}}$ and $Q^*_{g_{ff}}$ as dictated, respectively, by (34) and (35). To prove so, the experimental test presented above was repeated for the latter strategy, leading to a reduction of the 3rd, 5th and 7th order harmonics, respectively, down to 1.07%, 1.09% and 0.45% —see Fig. 8b—. Yet, as expected, the total active and reactive powers turned out being pulsating in return.

5.2. Robustness test against simultaneous disturbances and parameter deviations

So far, robustness of the global 2-SMC scheme against disturbances caused by wind variability has been evaluated. Nevertheless, aiming at complementing such a robustness assessment, the test presented in Section 5.1 was revisited after deliberately incorporating parameter deviations. For that purpose, the equivalent and ST control terms given, respectively, by (19), (48) and (20), (49) were calculated by intentionally assuming incorrect values for the rotor and stator resistors, as well as for the magnetising and line filter inductances. Specifically, resistances and inductances were respectively considered to be a 30% lower and a 30% higher than their actual values. This allowed testing robustness of the global control scheme without the need for physically modifying the laboratory prototype.

Figs. 9a and b show the performances of the RSC control variables obtained by adopting the same control parameter values and grid voltage conditions as those considered in Section 5.1. Similarly, Figs. 9c and d reflect those corresponding to the GSC control variables. It can be noticed that these signals do not practically vary from those obtained in the preceding section. Thus, not

only the robustness against disturbances conferred by 2-SMC is substantiated, but also its inherent robustness in the face of parameter variations and uncertainties. Both aspects of robustness are regarded to be mainly attributable to the non-parameter-dependent ST algorithm in (21) and (50).
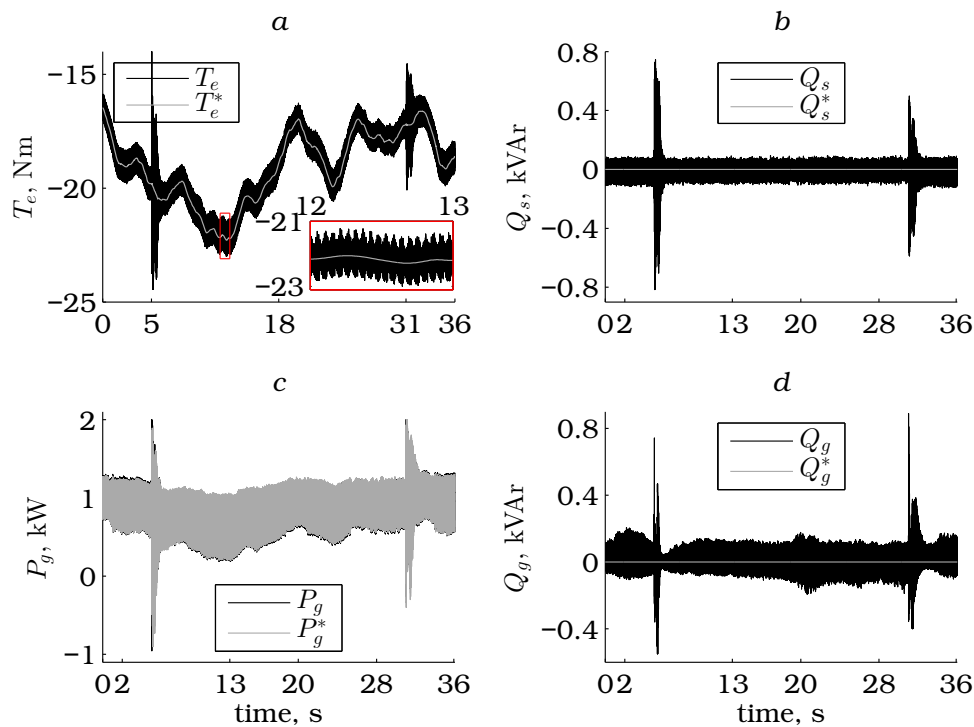

Fig. 9. *Control variables of the RSC and GSC 2-SMC algorithms under 30% simultaneous mismatches in resistances and inductances. **a** Electromagnetic torque. **b** Stator reactive power. **c** Gridside active power. **d** Grid-side reactive power.*

6. Conclusion

A comprehensive 2-SMC-based solution for controlling both the RSC and GSC of a wind turbine-driven DFIG has been put forward in this paper, which was expressly conceived to provide it with the capability of facing different types of grid voltage non-idealities, such as harmonic distortion and imbalances. Equations to assist the tuning of its control parameters have also been made available.

Although higher-order SMC theory rests on a rather convoluted mathematical basis, the resulting control algorithms have turned out being simple to implement and of a reasonable computational cost. Furthermore, in addition to leading to a fixed switching frequency of both the RSC and the GSC, the described approach delivers highly satisfactory performance in terms of tracking ability —a feature especially important when facing disturbed grid voltage scenarios—, dynamic response, and robustness against both parameter deviations and disturbances due to wind variability.

Moreover, the non-linear nature of 2-SMC, together with the tracking capability it confers, allow developing the complete control scheme as a function of stationary frame-referred magnitudes. The latter, in turn, makes possible entirely avoiding decomposition of the grid voltage and currents

in symmetrical sequences. As a consequence, the proposed control strategy is not valid just for a particular type of grid disturbance, but for dealing with diverse disturbed grid voltage profiles —e.g. harmonics of any degree, imbalances or even a combination of the two—, hence giving rise to a solution of remarkable versatility.

7. Acknowledgment

8. References

[1] Liserre, M., Cárdenas, R., Molinas, M., Rodríguez, J.: 'Overview of multi-MW wind turbines and wind parks', IEEE Trans. Ind. Electron., 2011, **58**, (4), pp. 1081–1095

[2] Mohamed, Y.A.-R.I.: 'Mitigation of dynamic, unbalanced, and harmonic voltage disturbances using grid-connected inverters with LCL filter', IEEE Trans. Ind. Electron., 2011, **58**, (9), pp. 3914–3924

[3] Hao, X., Yang, X., Liu, T., Huang, L., Chen, W.: 'A sliding-mode controller with multiresonant sliding surface for single-phase grid-connected VSI with an LCL filter', IEEE Trans. Power Electron., 2013, **28**, (5), pp. 2259–2268

[4] Xu, L., Wang, Y.: 'Dynamic modeling and control of DFIG-based wind turbines under unbalanced network conditions', IEEE Trans. Power Syst., 2007, **22**, (1), pp. 314–323

[5] Xu, L.: 'Coordinated control of DFIG's rotor and grid side converters during network unbalance', IEEE Trans. Power Electron., 2008, **23**, (3), pp. 1041–1049

[6] Hu, J., He, Y.: 'Reinforced control and operation of DFIG-based wind-power-generation system under unbalanced grid voltage conditions', IEEE Trans. Energy Convers., 2009, **24**, (4), pp. 905–915

[7] Hu, J., He, Y., Xu, L., Williams, B.W.: 'Improved control of DFIG systems during network unbalance using PI-R current regulators', IEEE Trans. Ind. Electron., 2009, **56**, (2), pp. 439–451

[8] Zhou, Y., Bauer, P., Ferreira, J.A., Pierik, J.: 'Operation of grid-connected DFIG under unbalanced grid voltage condition', IEEE Trans. Energy Convers., 2009, **24**, (1), pp. 240–246

[9] Hu, J., Nian, H., Xu, H., He, Y.: 'Dynamic modeling and improved control of DFIG under distorted grid voltage conditions', IEEE Trans. Energy Convers., 2011, **26**, (1), pp. 163–175

[10] Xu, H., Hu, J., He, Y.: 'Operation of wind turbine driven DFIG systems under distorted grid voltage conditions: Analysis and experimental validations', IEEE Trans. Power Electron., 2012, **27**, (5), pp. 2354–2366

[11] Shang, L., Hu, J.: 'Sliding-mode-based direct power control of grid-connected wind-turbine-driven doubly fed induction generators under unbalanced grid voltage conditions', IEEE Trans. Energy Convers., 2012, **27**, (2), pp. 362–373

[12] Zhou, P., He, Y., Sun, D.: 'Improved direct power control of a DFIG-based wind turbine during network unbalance', IEEE Trans. Power Electron., 2009, **24**, (11), pp. 2465–2474

[13] Abad, G., Rodríguez, M.A., Iwanski, G., Poza, J.: 'Direct power control of doubly-fed-induction-generator-based wind turbines under unbalanced grid voltage', IEEE Trans. Power Electron., 2010, **25**, (2), pp. 442–452

[14] Santos-Martin, D., Rodriguez-Amenedo, J.L., Arnaltes, S.: 'Direct power control applied to doubly fed induction generator under unbalanced grid voltage conditions', IEEE Trans. Power Electron., 2008, **23**, (5), pp. 2328–2336

[15] Santos-Martin, D., Rodriguez-Amenedo, J.L., Arnaltes, S.: 'Providing ride-through capability to a doubly fed induction generator under unbalanced voltage dips', IEEE Trans. Power Electron., 2009, **24**, (7), pp. 1747–1757

[16] Hu, J., Nian, H., Hu, B., He, Y., Zhu, Z.Q.: 'Direct active and reactive power regulation of DFIG using sliding-mode control approach', IEEE Trans. Energy Convers., 2010, **25**, (4), pp. 1028–1039

[17] Chen, S.Z., Cheung, N.C., Wong, K.C., Wu, J.: 'Integral sliding-mode direct torque control of doubly-fed induction generators under unbalanced grid voltage', IEEE Trans. Energy Convers., 2010, **25**, (2), pp. 356–368

[18] Utkin, V.I.: 'Sliding mode control design principles and applications to electric drives', IEEE Trans. Ind. Electron., 1993, **40**, (1), pp. 23–36

[19] Martinez, M.I., Tapia, G., Susperregui, A., Camblong, H.: 'Sliding-mode control for DFIG rotor- and grid-side converters under unbalanced and harmonically distorted grid voltage', IEEE Trans. Energy Convers., 2012, **27**, (2), pp. 328–339

[20] Martinez, M.I., Susperregui, A., Tapia, G., Xu, L.: 'Sliding-mode control of a wind turbine-driven double-fed induction generator under non-ideal grid voltages', IET Renew. Power Gener., 2013, **7**, (4), pp. 370–379

[21] Beltran, B., Benbouzid, M.E.H., Ahmed-Ali, T.: 'Second-order sliding mode control of a doubly fed induction generator driven wind turbine', IEEE Trans. Energy Convers., 2012, **27**, (2), pp. 261–269

[22] Susperregui, A., Martinez, M.I., Zubia, I., Tapia, G.: 'Design and tuning of fixed-switching-frequency second-order sliding-mode controller for doubly fed induction generator power control', IET Electr. Power Appl., 2012, **6**, (9), pp. 696–706

[23] Msaddek, A., Gaaloul, A., M'Sahli, F.: 'Comparative study of higher order sliding mode controllers'. Proc. 15th IEEE International Conference on Sciences and Techniques of Automatic Control and Computer Engineering (STA), Hammamet, Tunisia, December 2014, pp. 915–922

[24] Young, K.D., Utkin, V.I., Özgüner, Ü.: 'A control engineers guide to sliding mode control', IEEE Trans. Control Syst. Technol., 1999, **7**, (3), pp. 328–341

[25] Susperregui, A., Martinez, M.I., Tapia, G., Vechiu, I.: 'Second-order sliding-mode controller design and tuning for grid synchronisation and power control of a wind turbine-driven doubly fed induction generator', IET Renew. Power Gener., 2013, **7**, (5), pp. 540–551

[26] López, J., Sanchis, P., Roboam, X., Marroyo, L.: 'Dynamic behavior of the doubly fed induction generator during three-phase voltage dips', IEEE Trans. Energy Convers., 2007, **22**, (3), pp. 709–717

[27] Utkin, V., Guldner, J., Shi, J.: 'Sliding mode control in electromechanical systems' (Taylor & Francis, 1999, 2nd edn.)

[28] Levant, A.: 'Sliding order and sliding accuracy in sliding mode control', Int. J. Control, 1993, **58**, (6), pp. 1247–1263

[29] Senturk, O.S., Hava, A.M.: 'A simple sag generator using SSRs', IEEE Trans. Ind. Appl., 2012, **48**, (1), pp. 172–180

[30] Guasch, L., Córcoles, F., Pedra, J.: 'Effects of symmetrical and unsymmetrical voltage sags on induction machines', IEEE Trans. Power Del., 2004, **19**, (2), pp. 774–782

[31] Tsili, M., Papathanassiou, S.: 'A review of grid code technical requirements for wind farms', IET Renew. Power Gener., 2009, **3**, (3), pp. 308–332

[32] Muyeen, S.M., Hasan Ali, Md., Takahashi, R., Murata, T., Tamura, J., Tomaki, Y., Sakahara, A., Sasano, E.: 'Comparative study on transient stability analysis of wind turbine generator system using different drive train models', IET Renew. Power Gener., 2007, **1**, (2), pp. 131–141

[33] Martinez, M.I., Tapia, G., Susperregui, A., Camblong, H.: 'DFIG power generation capability and feasibility regions under unbalanced grid voltage conditions', IEEE Trans. Energy Convers., 2011, **26**, (4), pp. 1051–1062